PERGAMON International Journal of Multiphase Flow 28 (2002) 451–477

International Journal of Multiphase Flow

www.elsevier.com/locate/ijmulflow

# Multiphase flow with impinging droplets and airstream interaction at a moving gas/solid interface

G.F. Naterer *

*Department of Mechanical and Industrial Engineering, University of Manitoba, 25 Gillson Street, Winnipeg, Manitoba, Canada R3T 2N2*

Received 24 October 2000; received in revised form 18 October 2001

**Abstract**

Multiphase flows with droplets involving gas (air), liquid (droplets) and solid (ice) phases are examined in this paper. The external multiphase flow is predicted in conjunction with a moving phase interface arising from solidification of impinging supercooled droplets. A scalar transport form of the droplet flow equations is solved separately from the viscous main (air) flow solver. This approach provides an effective alternative to tracking of individual droplet trajectories in the freestream. Interactions between the droplet and main (air) flows appear through appropriate inter-phase expressions in the momentum balance equations within each individual phase. The numerical formulation is based on a CVFEM (Control-Volume-based Finite Element Method) with quadrilateral isoparametric elements. This model is applied to problems involving the formation of rime (dry) ice (i.e., without liquid film covering the ice surface). Experimental data provides further insight into the impingement of droplets on a cylindrical conductor. Favorable agreement between the numerical and experimental results is achieved. © 2002 Elsevier Science Ltd. All rights reserved.

## 1. Introduction

Droplet flows with phase change arise in many engineering applications, i.e., atmospheric icing of structures and aircraft, spray deposition and splat-quenched solidification in manufacturing and materials processing, combustion, etc. In particular, freezing precipitation can cause serious damage to many types of structures, including overhead power transmission lines and telecommunication towers. In addition to major potential damage during severe storms (i.e., ice and wind loads damaging structures and disrupting power supply), lighter icing occurs more frequently. In

---

* Tel. : +1-204-474-9804; fax: +1-204-275-7507.
*E-mail address:* natererg@cc.umanitoba.ca (G.F. Naterer).

PII: S0301-9322(01)00076-3

the case of power transmission, the accumulated ice shape may lead to large aerodynamic forces on the power lines as a result of the streamlined resemblance between an iced conductor and an aircraft wing. The resulting aerodynamic wind loads may then produce unstable flow-induced vibrations (called galloping) with resulting forces much larger than forces arising from the ice weight alone. Significant contributions in the understanding of these ice processes have been reported by Lu et al. (1998), as well as others (i.e., Desai et al., 1996). Galloping has been long recognized and discussed in relation to the design of power transmission systems (Fink and Beaty, 2000; ASCE, 1991; Nigol and Havard, 1978). In the present context, these scenarios have been recognized in the design of power transmission systems at Manitoba Hydro, Canada.

In this paper, modelling of multiphase flow in three-phase conditions (air, droplets and ice simultaneously) is considered. This involves the problem of tracking impinging droplets at the ice surface. The ice accretion is affected by the rate at which the main (air) flow carries droplets onto the ice surface. The impinging droplet flux can be integrated around the conductor in a mass conservation balance to predict the ice growth rate (i.e., Goodwin et al., 1982). In rime (dry) ice conditions, the supercooled droplets freeze immediately upon impact (Poots, 1996), whereas droplet runback as a liquid film along the surface occurs in wet (glaze) ice conditions (Myers and Hammond, 1999; Naterer et al., 1999). In both cases, predictions of the impinging droplets require understanding of the external multiphase flow and its interaction with the moving ice interface along the solid boundary. Inter-phase forces and mass exchange processes involving air and droplets may be examined through appropriate time and spatial averaging of the continuum equations (Banerjee and Chan, 1980; Tsuboi and Kimura, 1998). In this work, both numerical and experimental results are examined for better understanding of rime ice processes.

A primary difficulty in this multiphase flow problem involves the prediction of the unknown position of the ice–air interface during the simultaneous solutions of the droplet and main (air) flow equations. A combined momentum integral and panel method has been used to predict the external air flow field in the presence of ice accretion (Draganoiu et al., 1996). As droplets arrive on the ice surface, the advancing interface must properly balance this incoming mass flux. In practice, this balance requires special treatment of the phase interface advance once a control volume along the ice surface is ‘filled’ (i.e., filled with incoming droplets and/or surface ice). Conventional iterative techniques for moving boundary problems typically involve iterations in terms of phase fraction, but in our case, the control volume on the accreting ice surface requires an additional mechanism to prevent excess mass influx from ‘overfilling’ control volumes at the edge of the ice–air interface. It is anticipated that convergence difficulties would be observed with conventional iterative solutions of this problem. Furthermore, free surface models with deforming grids likely would involve more complexity and computational effort than required in the current problem. Other techniques, such as an apparent specific heat in solid–liquid phase change analysis (Naterer and Schneider, 1995), alone do not directly solve the problem of droplet mass overfilling in a control volume with subsequent accumulation in adjacent volumes due to the external droplet flow. As a result, the development of innovative solution techniques is required for effective modelling of multiphase flows involving air, droplets and a moving ice–air interface, simultaneously.

In the current work, a novel approach is presented to predict ice accretion on a conductor under various environmental conditions. This three-phase approach (air, droplets and ice simultaneously) involves the main (air) flow and droplet equations, together with droplet impact and phase change on the ice surface, as modelled by a CVFEM (Control-Volume-based Finite Element Method). This formulation is unique with respect to its ability to permit simultaneous computations of ice accretion with deflection of external droplets due to the viscous main (air) flow past the moving ice surface. These numerical predictions will be compared and assessed in conjunction with experimental data involving ice weight and shape as observed in experiments with a freezing rain simulator.

## 2. Problem formulation

The governing equations for multiphase flow with droplets may be obtained through spatial averaging of the individual phase equations over a control volume containing a mixture of phases (i.e., solid, liquid and air). Mathematical formulations for multiphase flows have been documented by various authors, including Banerjee and Chan (1980), as well as Lahey and Drew (1979, 1993). In this Eulerian approach, a uniform spatial droplet distribution is assumed within each control volume. Furthermore, spatially averaged approximations are adopted for cross-phase processes, such as momentum and thermal interactions between the droplets and main (air) flow. It will be shown that the conservation equations for this multiphase flow can be derived as special cases of the following conservation equation for a general scalar quantity.

### 2.1. General scalar equation

Consider the transport of a scalar quantity, $\phi_k$, associated with phase $k$ in a control volume containing a mixture of phases at a differential level (see Fig. 1). The conservation equation for $\phi_k$ may be written as

$$\frac{\partial(\rho_k\phi_k)}{\partial t}+\frac{\partial(\rho_k\phi_k u_k)}{\partial x}+\frac{\partial(\rho_k\phi_k v_k)}{\partial y}+\frac{\partial(\mathbf{j}_{k,x})}{\partial x}+\frac{\partial(\mathbf{j}_{k,y})}{\partial y}=\hat{S}_k. \tag{1}$$

In Eq. (1), the component terms represent the transient accumulation of $\phi_k$ in the control volume occupied by phase $k$, the net advection flow of $\phi$ across the phase $k$ portion of the control surface (second and third terms), the net diffusion flow into phase $k$ across the interfacial surface (fourth and fifth terms), and the source or sink of $\phi_k$ (i.e., the contributions due to evaporation, etc.) in

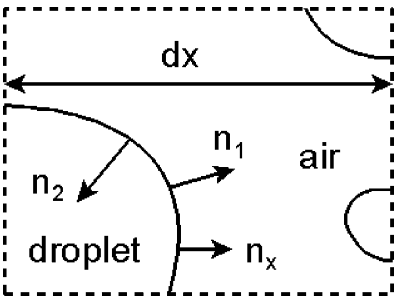

Fig. 1. Control volume with mixture of phases.

the phase $k$ portion of the control volume, respectively. The velocity of phase $k$, denoted by $\mathbf{v}_k$ (note: vectors have bold font), consists of scalar components in the $x$ direction ($u_k$) and $y$ direction ($v_k$).

The interfacial balances are further described with reference to Fig. 1. The following symbols are adopted: $a$ refers to surface area (per unit volume), $\mathbf{n}_x$ is the outward normal ($x$ direction), $\mathbf{j}_k$ refers to the diffusive flux of the conserved quantity, $V_k$ is the volume of phase $k$ and $\mathbf{v}_i$ denotes the interface velocity. In order to derive the volume averaged form of the governing equation, Eq. (1), the following Leibnitz and Gauss rules are required:

$$\frac{\partial}{\partial t}\int_{V_k} B\,\mathrm{d}V = \int_{V_k}\frac{\partial B}{\partial t}\,\mathrm{d}V + \int_a B(\mathbf{v}_i\cdot\hat{\mathbf{n}}_k)\,\mathrm{d}S \quad \text{(Leibnitz)}, \tag{2}$$

$$\int_{V_k}\nabla\cdot\mathbf{b}\,\mathrm{d}V = \frac{\partial}{\partial\mathbf{x}}\int_{V_k}\hat{\mathbf{n}}_{\mathbf{x}}\cdot\mathbf{b}\,\mathrm{d}V + \int_a(\hat{\mathbf{n}}_k\cdot\mathbf{b})\,\mathrm{d}S \quad \text{(Gauss)}, \tag{3}$$

where $B$ and $\mathbf{b}$ refer to arbitrary scalar and vector quantities, respectively.

A volume averaged form of Eq. (1) conveniently accommodates a control volume that contains droplets having a spectrum of somewhat different diameters. Moreover, impinging droplets may freeze along the ice surface (i.e., solid, liquid and air phases may occur simultaneously), thereby making individual droplet tracking difficult. As a result, it is convenient to identify a volume averaged quantity in the following manner:

$$\langle\beta_k\rangle = \frac{1}{V_k}\int_{V_k}\beta_k\,\mathrm{d}V. \tag{4}$$

Also, the phase volume fraction is defined as

$$C_k = \frac{V_k}{V}. \tag{5}$$

This volume fraction can be written in terms of a mass fraction through appropriate multiplication by density.

The volume averaged form of Eq. (1) is obtained by integration of the governing equation over $V_k$. Following this volume averaging of Eq. (1), together with Eqs. (2) and (3),

$$\frac{\partial}{\partial t}C_k\langle\rho_k\phi_k\rangle + \frac{\partial}{\partial x}C_k\langle\hat{\mathbf{n}}_x\cdot(\rho_k\phi_k\mathbf{v}_k+\mathbf{j}_k)\rangle + \frac{\partial}{\partial y}C_k\langle\hat{\mathbf{n}}_y\cdot(\rho_k\phi_k\mathbf{v}_k+\mathbf{j}_k)\rangle + \frac{1}{V}\int_a(\dot{m}_k''\phi_k+\mathbf{j}_k\cdot\hat{\mathbf{n}}_k)\,\mathrm{d}S = C_k\langle\hat{S}_k\rangle. \tag{6}$$

The $\dot{m}_k''$ term refers to the inter-phase mass flux (units of mass per unit time and area). In Eq. (6), special care is required in the interpretation of the area integration in the last term on the left-hand side of this equation. The symbol $\int_a$ refers to integration over the total area, including the interfacial area per unit volume (i.e., $a_i$ along the boundary separating two distinct phases within the control volume), and any area of phase $k$ in contact with the external walls, $a_w$, or boundaries of the system (per unit volume). Typically, the $\dot{m}_k''$ term becomes zero upon evaluation along the walls due to zero velocity conditions there. However, for the interfacial part of the surface integration, this $\dot{m}_k''$ term may involve evaporation or coalescence effects (mass equation) or force implications (momentum equations). In any event, the area integration involves a sum including $a_w$ and $a_i$ and consideration of both components is important in the subsequent derivation of the individual conservation equations.

The general scalar transport equation can now be applied to multiphase flows with droplets. However, before the resulting equations of motion are examined, consider the various approaches (benefits and disadvantages) in handling multiphase problems. In multiphase flows with droplets and phase change, there are three main types of methods to predict the main and droplet flows: (i) mixture model, (ii) tracking of individual droplet trajectories and (iii) three-phase (Eulerian) model. In the mixture approach, the droplet and air phases are treated as a homogeneous mixture within a discrete (or differential) control volume. In this way, a single velocity is sought which represents the mean velocity of the droplet and air mixture. This approach is widely adopted in other two-phase problems, most notably problems involving solid–liquid phase change, since the velocity in one phase is well known (i.e., stationary solid phase), so the other phase velocity can be readily determined from the mixture velocity. However, in multiphase flows with droplets, this type of approach is limited in the sense that it is usually difficult to subdivide the components of mixture velocity into their respective phases.

In the second (Lagrangian) approach, individual droplet trajectories are tracked through the flow field. A force balance is used on each individual droplet, together with an appropriate empirical estimate of the drag coefficients, to find the resulting droplet acceleration (and thus velocity through time integration). In addition to the complexity of tracking very many droplets, this approach is also difficult to implement into existing computer codes involving a fixed domain and mixture quantities located at the nodes of a finite element/volume mesh.

In an Eulerian approach, the droplet and air phases are individually averaged spatially throughout the control volume and the resulting transport equations are solved for these individual phase equations. Interactions between the phases are handled through appropriate phase interaction terms, such as spatially averaged force interactions between the air and droplet phases in the momentum equations. In this way, the benefits of the mixture model (reduced computational time) and droplet tracking approach (capturing inter-phase interactions) can be effectively retained, while providing a framework for implementation into existing fixed domain codes. In particular, the three-phase approach allows the droplet flow equations to be written in a standard scalar transport form in conjunction with gas (air), liquid (droplet) and solid phases (moving ice interface) simultaneously.

### 2.2. Mass equation

In this case, set $\phi_k = 1$, $\mathbf{j}_k = 0$ and $\hat{S}_k = 0$ in Eq. (6) to obtain the following result:

$$\frac{\partial}{\partial t} C_k \langle \rho_k \rangle + \frac{\partial}{\partial x} C_k \langle \rho_k u_k \rangle + \frac{\partial}{\partial y} C_k \langle \rho_k v_k \rangle + \langle \dot{m}_k'' \rangle_i = 0, \tag{7}$$

where the subscript $i$ refers to evaluation across the interfacial area of the control volume. In general, the volume averaged, interfacial mass flux of droplets arises from evaporation, etc. It is typically not well known so a suitable correlation must be supplied. The subscript $k$ refers to phase $k$, and in the case of the liquid phase, $u_k$ refers to an effective (spatially averaged) droplet velocity in the $x$ direction.

Now $\hat{\rho}_l$ is defined as a mass of water (droplets) per unit volume of the water–air mixture, where

$$\hat{\rho}_l = \frac{m_l}{V} = C_k\langle\rho_k\rangle. \tag{8}$$

Alternatively, $\hat{\rho}_k$ is called the *liquid water content*; it is analogous to the concept of humidity except that it includes discrete droplets rather than a continuous mixture of moisture in the air. The hat notation in Eq. (8) is used to distinguish liquid density (i.e., density of liquid water is 1000 kg/m$^3$) from the concept of liquid water content, which refers to the mass of liquid phase (droplets) in a control volume occupied by both liquid and air. The subscript is still relevant since it refers to the content of liquid (rather than air) in the multiphase control volume.

Combining Eqs. (7) and (8) for the liquid (droplet) phase:

$$\frac{\partial\hat{\rho}_l}{\partial t} + \frac{\partial(\hat{\rho}_l u_l)}{\partial x} + \frac{\partial(\hat{\rho}_l v_l)}{\partial y} + \langle\dot{m}_l''\rangle_i = 0. \tag{9}$$

Droplet evaporation and coalescence, which are represented by $\dot{m}_l''$ in Eq. (9), are assumed to be small in comparison to the other mass inflow/outflow terms. Also, the processes of evaporation and coalescence are indirectly incorporated since an equivalent droplet mass is approximated within the specified mean droplet diameter. Details involving spatial averaging in the derivation of Eq. (9) are shown by Tsuboi and Kimura (1998) for similar conditions in incompressible droplet flows. It can be observed that the form of Eq. (9) is similar to the regular continuity equation. It may be considered in an analogous way as a species transport equation, whereby the 'concentration' of droplets (or phase fraction) is tracked throughout the flow field.

The volume fraction, $C_l$, can be calculated in terms of $\hat{\rho}_l$ following multiplication by $\rho_l$ (or $\rho_w$; the density of water). As a result, the governing equation can be divided by $\rho_l$ to obtain a transport equation for the volume fraction of droplets occupying a droplet–air control volume. An additional phase fraction, $\lambda$, can also be introduced to distinguish liquid and solid phases when droplet freezing (or ice melting) occurs along the ice surface.

It can be observed that the average of a product in Eq. (7), given by $\langle\rho_k u_k\rangle$, has been transformed to a product of averaged quantities in Eq. (9). In order to perform this transformation, a distribution coefficient for the product of $\rho_k$ and a general scalar quantity, $\phi_k$, is defined as follows:

$$\chi_k = \frac{\langle\rho_k\phi_k\rangle}{\langle\rho_k\rangle\langle\phi_k\rangle}. \tag{10}$$

In multiphase flows involving a dispersed phase (i.e., droplets dispersed uniformly within air flow), it is generally assumed that the phase density variations within the averaging volume are sufficiently small so that the distribution coefficient is approximately equal to one (Banerjee and Chan, 1980). Very little or no data involving distribution coefficients for multiphase flows in the present context is available in the technical literature, and so setting these coefficients to one is often practised (Banerjee and Chan, 1980). Furthermore, these coefficients have been predicted theoretically as $\chi_k \approx 1$ under most practical circumstances by using power low profiles for the flow quantities (Bankoff, 1960). As a result, the separation of variables into a product of averaged quantities is adopted in Eq. (9), as well as similar transformations in the following momentum equations.

### 2.3. Momentum equations

In this case, set $\phi_k = \mathbf{v}_k$, $\mathbf{j}_k = p_k\mathbf{I} - \tau_k$, and $\hat{S}_k = \mathbf{G}_k$, where $\mathbf{I}, \tau_k$ and $\mathbf{G}_k$ refer to the identity matrix, stress tensor and body and/or inter-phase forces, respectively. Also, the component of the resulting equation (6) in the $x$ direction is obtained by taking the dot product of this equation with the unit $x$ direction vector, $\hat{\mathbf{n}}_x$. For example, the convective and pressure terms of the $x$ direction momentum equation are transformed by

$$\mathbf{n}_x \cdot \frac{\partial}{\partial x} C_k \langle \mathbf{n}_x \cdot (\rho_k \mathbf{v}_k \mathbf{v}_k) \rangle = \mathbf{n}_x \cdot \frac{\partial}{\partial x} C_k \langle \rho_k u_k \mathbf{v}_k \rangle = \frac{\partial}{\partial x} C_k \langle \rho_k u_k^2 \rangle, \tag{11}$$

$$\mathbf{n}_x \cdot \frac{\partial}{\partial x} C_k \langle \mathbf{n}_x \cdot p_k \mathbf{I} \rangle = \frac{\partial}{\partial x} C_k \langle p_k \rangle \tag{12}$$

since $\mathbf{I} \cdot \mathbf{n}_x = \mathbf{n}_x$ and $\mathbf{n}_x \cdot \mathbf{n}_x = 1$. Similar operations are performed on the stress tensor terms obtained in Eq. (6). Furthermore, the right-hand side of Eq. (6) involves the cross-phase interactions of pressure and shear stress at the interfacial portion of the boundary, which is modelled through a term denoted by $G_{x,k}$.

After each term is assembled into Eq. (6)

$$\begin{aligned} &\frac{\partial}{\partial t} C_k \langle \rho_k u_k \rangle + \frac{\partial}{\partial x} \left[ C_k \langle \rho_k u_k^2 \rangle + \rho_k \langle \hat{\mathbf{n}}_x \cdot (\tau_k \cdot \hat{\mathbf{n}}_x) \rangle \right] + \frac{\partial}{\partial y} \left[ C_k \langle \rho_k u_k v_k \rangle + \rho_k \langle \hat{\mathbf{n}}_x \cdot (\tau_k \cdot \hat{\mathbf{n}}_k) \rangle \right] \\ &\quad = -\frac{\partial}{\partial x} C_k \langle p_k \rangle - \frac{1}{V} \int_a \{ \dot{m}_k u_k + \hat{\mathbf{n}}_x \cdot (\hat{\mathbf{n}}_k p_k) - \hat{\mathbf{n}}_x \cdot (\hat{\mathbf{n}}_k \cdot \tau_k) \} \, \mathrm{d}S + C_k \langle G_{x,k} \rangle. \end{aligned} \tag{13}$$

Similar equations for the momentum equations in the $y$ and $z$ directions are obtained by taking the dot product with respect to $\hat{\mathbf{n}}_y$ and $\hat{\mathbf{n}}_z$, respectively.

The phase interaction forces are typically combined with other interfacial forces, such as the $\tau_k$ terms, using some form of resistance law for the droplets. The following interfacial expression can be adopted (Hewitt et al., 1997):

$$G_{x,k} = \frac{18\mu_a}{d^2} \frac{c_\mathrm{d} Re_l}{24} (u_a - u_l), \tag{14}$$

where $Re_l = \rho_g |u_a - u_l| d / \mu_a$ is the droplet's Reynolds number (based on the relative velocity) and $d$ is the mean droplet diameter in the flow. Other researchers (i.e., Tsuboi and Kimura, 1998) have modified the resistance force between the air and droplet streams such that it becomes proportional to the velocity difference (between air and droplet) raised to an exponent $\gamma$ (empirical factor), rather than the difference alone. It may be shown that as the droplet inertia increases, its trajectory is less altered by the air flow near the ice surface. In the current approach, the exponentiated resistance force term leads to this anticipated trend in the droplet flow dynamics.

Assuming a spherical shape for each droplet, the following curve fit may be used for the drag coefficient (Szilder et al., 1987):

$$c_\mathrm{d} = \frac{24}{Re_l} + \frac{4.73}{Re_l^{0.37}} + 0.00624 Re_l^{0.38}. \tag{15}$$

Although this correlation is adopted over the entire range of Reynolds numbers, it is generally considered to be valid up to $Re_l = 3 \times 10^5$, which is well within the range of the current droplet flows since $Re_l$ is based on the relative velocity, not the absolute velocity. Eqs. (14) and (15) are not adopted in the usual fashion in control volumes along the moving boundary (ice–air), since the solid fraction there reduces the effective volume which encompasses the air/droplet interactions. It is assumed that the droplets remain dispersed until they reach the ice interface, since in the present study, rime (dry) ice is assumed such that droplets adhere immediately upon impact, without splashing off the surface. Only the force within the air/droplet portion of the control volume is incorporated since the inter-phase resistance term (right-hand side of Eq. (13)) involves the phase fraction (in $C_k$) multiplied by $G_{x,k}$. As a result, the force between air/droplets is included in the non-ice portion of the control volume, and a zero force (due to zero velocities) arises in the solid (ice) portion of the control volume.

The droplet flow is sustained mainly by forces imparted on each droplet from the main (air) flow, rather than by internal pressure gradients within the droplet. The main forces are handled through the above resistance law (note: in addition to gravitational forces for the $y$ direction equation). As a result, in the liquid (droplet) phase,

$$\frac{\partial(\hat{\rho}_l u_l)}{\partial t} + \frac{\partial(\hat{\rho}_l u_l u_l)}{\partial x} + \frac{\partial(\hat{\rho}_l u_l v_l)}{\partial y} + \langle \dot{m}_l'' u_l \rangle = C_l \langle G_{x,l} \rangle \tag{16}$$

can be derived in a manner similar to that of Eq. (9). Further specific details involving spatial averaging are described by Tsuboi and Kimura (1998), as well as Banerjee and Chan (1980), under similar conditions for multiphase flows.

For the $y$ direction momentum equation, an additional gravity term appears in the negative $y$ direction for the corresponding form of Eq. (16). In this way, a droplet falls under its own weight. Also, the pressure gradient term appears in the corresponding Navier–Stokes equations for the main (air) flow. In particular, Eq. (16) is obtained for the liquid (droplet) phase, whereas substitution of the phase subscript ($k$) as the gas (air) phase yields the main (air) flow equations. After $\hat{\rho}_l$ (or $C_l$) are obtained from a computational solution of Eq. (9), then Eq. (16) and an analogous $y$ direction equation are solved in conjunction with suitable inter-equation iterations to give the components of droplet velocities, $u_l$ and $v_l$.

### 2.4. Energy equation

In the case of heat transfer, let $e_k = \phi_k = \hat{e}_k + \frac{1}{2}\mathbf{v}_k \cdot \mathbf{v}_k$ (total energy), $\mathbf{j}_k = \mathbf{q}_k + (p_k \mathbf{I} - \tau_k) \cdot \mathbf{v}_k$ (Fourier heat flux and work contributions arising from pressure and viscous forces) and $\hat{S}_k = \mathbf{F}_{b,k} \cdot \mathbf{v}_k + \hat{S}_{k,e}$ (work contributions arising from body forces, such as gravity, and heat generated per unit volume). In this way, heat transfer between the droplets and air stream can be predicted. However, the present work assumes that the droplet temperature matches the air temperature in the freestream and then changes to the phase change temperature upon impact and solidification on the ice surface. The phase change temperature can vary, depending on ambient conditions such as the freestream pressure. The current type of ice formation is called rime (dry) ice and it typically occurs at ambient temperatures below about −5 °C (Poots, 1996) in structural icing problems. However, transition from rime ice to glaze ice typically occurs at much lower temperatures (i.e., aircraft icing).

The following list summarizes the governing equations to be solved for multiphase flow with incoming droplets at the ice surface:

- Eq. (9) for the volume fraction (or mass fraction) of droplets,
- Eq. (16) and corresponding Navier–Stokes equations for droplet and air velocity fields, respectively.

In the following section, the numerical approximation of these governing equations will be described.

## 3. Numerical formulation

Since analytical solutions of the previously described multiphase flow equations are generally not available, a numerical solution is often required. This numerical solution involves discretization of the problem domain, as well as the previously described governing equations. In this section, the method of spatial discretization based on a CVFEM is presented. The CVFEM combines the geometric flexibility of the finite element method with the important conservation based properties (i.e., enforcement of mass, energy conservation) of the finite volume procedure.

### 3.1. Discretization of solution domain

The solution domain is subdivided into an assembly of isoparametric quadrilateral elements. Each finite element is further subdivided into a set of sub-control-volumes (SCVs). Then, after assembly of all elements, a finite volume is established by all sub-volumes associated with a particular node (see Fig. 2). Local coordinates, $s$ and $t$, are used within each element and integration points (ips) are defined at the midpoint of each sub-surface (SS) for evaluation of surface flux terms, such as the mass flux, in the control volume equations.

Then, bilinear shape functions are used for global to local coordinate transformations and interpolation of scalar values in the domain. For example, the value of a general scalar quantity, $\phi$, at the local coordinate, $(s, t)$, is approximated by

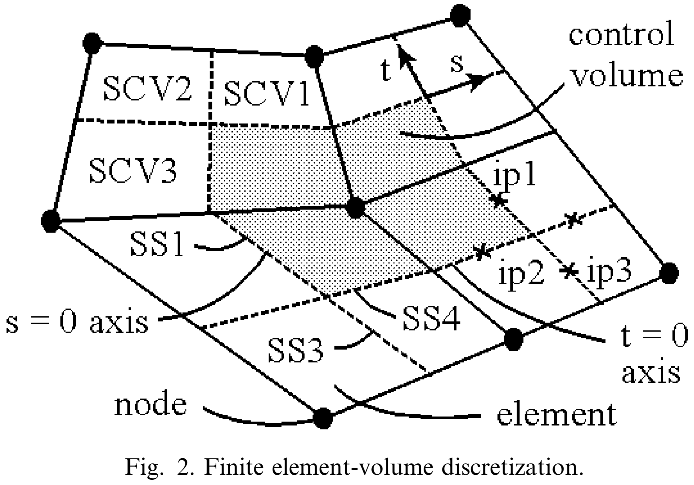

Fig. 2. Finite element-volume discretization.

$$\phi(s,t) = \sum_{i=1}^{4} N_i(s,t)\Phi_i, \tag{17}$$

where the shape functions, $N_i$, are given by

$$N_1(s,t) = \frac{1}{4}(1+s)(1+t), \tag{18}$$

$$N_2(s,t) = \frac{1}{4}(1-s)(1+t), \tag{19}$$

$$N_3(s,t) = \frac{1}{4}(1-s)(1-t), \tag{20}$$

$$N_4(s,t) = \frac{1}{4}(1+s)(1-t), \tag{21}$$

and the subscripts $i = 1, 2, 3$ and 4 refer to local nodes. It should be noted that $t$ refers to the local coordinate only in Eqs. (17)–(21); otherwise (everywhere else in this paper), it refers to time.

### *3.2. Control volume equations*

In addition to spatial discretization of the problem domain, a suitable discretization of the multiphase flow equations must be provided. This discretization is based on earlier numerical formulations involving fluid flow and phase change heat transfer (i.e., Naterer and Schneider, 1995). Various approaches have been developed for the numerical analysis of multiphase flows with droplets; these developments have largely arisen from applications such as droplet combustion and chemically reacting flows. In many cases, the main issues in such applications deal with interactions between the droplet flow and the surrounding flow field. For example, turbulence in the freestream affects the mixing and reaction rates of droplets in an internal combustion engine. Consequently, computational models then typically involve detailed droplet tracking algorithms to predict the sub-grid heat transfer rates due to droplet evaporation and combustion. However, in the current work, an important focus is accumulation and solidification of impinging droplets on the contact surface, with less emphasis on the droplet–gas interaction in the freestream. As a result, an alternative model that is based on an Eulerian formulation is considered here. In addition to retaining effective modelling in the freestream, it is anticipated that computational demands, which essentially arise from various features of conventional fine-scale droplet tracking, may be reduced.

The discrete form of the governing equations may be obtained by integration of the conservation equation, Eq. (1), over a discrete volume, with the result that

$$\int_A \frac{\partial(\rho_k \phi_k)}{\partial t}\,\mathrm{d}A + \int_S (\rho_k \phi_k \mathbf{v}_k)\cdot \mathbf{dn} + \int_S (\mathbf{j}_k)\cdot \mathbf{dn} = \int_A \hat{S}_k\,\mathrm{d}A, \tag{22}$$

where $A$ and $S$ refer to the area of the shaded region in Fig. 2 and surface length traversed around the outer edge of this area, respectively (note: $A$ and $S$ become volume and surface area in 3-D problems).

An implicit formulation is adopted here; in other words, convection, diffusion and source terms in Eq. (22) are evaluated at the current time level rather than a previous time level in an explicit approach. In this way, larger time steps can be taken in the simulations while retaining numerical stability, thereby reaching a fixed point in time with reduced computational effort (in comparison to explicit scheme). In view of the complicated interaction between the droplet flow, continuity and multiphase momentum equations in the present formulation, the ability to reliably obtain converged results at each time step in a cost effective manner was an important motivation in adopting an implicit formulation.

With reference to SCV1, a backward difference in time is adopted for the approximation of the first term in Eq. (22), i.e.,

$$\int_{\mathrm{SCV1}} \frac{\partial(\rho_k \phi_k)}{\partial t}\,\mathrm{d}A \approx J_1\left[\frac{(\rho_k \Phi_k)_1^{n+1} - (\rho_k \Phi_k)_1^{n}}{\Delta t}\right], \tag{23}$$

where $J_1$ refers to Jacobian (i.e., area of SCV1). Also, the subscript 1 and superscript $n$ refer to local node 1 and previous time level, respectively. In Eq. (23), the upper case $\Phi$ refers to a value calculated at the node of a finite element, whereas the lower case $\phi$ would mean that the value is computed internally within the element (i.e., at the integration point). For example, $u$ would refer to evaluation at the integration point, whereas $U$ refers to nodal velocity (see Fig. 2 for illustration showing integration point and nodal locations).

A similar lumped approximation is adopted for the source (right-hand side) term in Eq. (22),

$$\int_{\mathrm{SCV1}} \hat{S}_k\,\mathrm{d}A \approx J_1(\hat{S}_k)_{1/2,1/2}, \tag{24}$$

where the 1/2, 1/2 subscript refers to the local coordinate position (i.e., center of SCV1).

The convective term in Eq. (22) requires evaluation at both SS1 and SS4 sub-surfaces since both surfaces contribute to the convective transport of $\phi$ in the SCV1 conservation equation. In the case of the SS1 evaluation

$$\int_{\mathrm{SS1}} (\rho_k \phi_k \mathbf{v}_k)\cdot \mathbf{dn} \approx (\rho_k \phi_k u_k)_{\mathrm{ip1}}\Delta y_1 - (\rho_k \phi_k v_k)_{\mathrm{ip1}}\Delta x_1. \tag{25}$$

A similar expression is obtained for the SS4 integration. Since an implicit formulation is used, inter-equation iterations (involving conservation equations for mass, momentum, etc.) are required to handle the non-linear convection term in Eq. (25). For example, in the momentum equation, the convective terms in Eq. (25) involve a *convected* velocity (a linearized or lagged velocity) multiplied by a *convecting* velocity (active velocity obtained through integration point equations). Iterative updates are required following each solution of the linearized flow equations until suitable convergence is achieved between both velocities.

The diffusive term is evaluated at both SS1 and SS4 surfaces. In the SS1 approximation

$$\int_{S} (\mathbf{j}_k)\cdot \mathbf{dn} \approx \mathbf{j}_{k,x}|_{\mathrm{ip1}}\Delta y_1 - \mathbf{j}_{k,y}|_{\mathrm{ip1}}\Delta x_1, \tag{26}$$

where the midpoint approximation has been adopted again. The flux term, $\mathbf{j}_k$, can be related to the scalar variable, $\phi_k$, through a suitable phenomenological law. For example, in the case of energy conservation, it represents the Fourier heat flux, and so the resulting diffusive term can be approximated as

$$\int_S (\mathbf{j}_k) \cdot \mathbf{dn} \approx -\kappa\left(\sum_{i=1}^{4} \frac{\partial N_i}{\partial x} T_i\right)\Delta y_1 + \kappa\left(\sum_{i=1}^{4} \frac{\partial N_i}{\partial y} T_i\right)\Delta x_1, \tag{27}$$

where $\kappa$ refers to thermal conductivity.

After Eqs. (23)–(26) are substituted into Eq. (22), an equation involving nodal and integration point values of $\phi$ (such as velocity), as well as integration point velocities (to be determined), is obtained. However, in reference to Fig. 2, these terms only represent the SCV1 portion of the entire control volume. The full control volume equation, Eq. (22), is completed after all elements are assembled since the sub-volume contributions to a conservation equation for a particular global node are completed after all elements are considered. In a computer program, a loop would be carried out over all finite elements, and within this loop, all component terms from Eqs. (23)–(26) would be evaluated at each sub-surface (another inner loop). These terms are added to the appropriate row and column of the global matrix which corresponds to the node of that particular SCV. The leading coefficients in front of $\phi$ (convection and diffusion terms) are stored in the global matrix since an implicit method is adopted, and the transient and source term parts of Eq. (22) are stored on the right-hand side. This procedure yields a banded matrix of equations to be solved for the nodal unknowns.

However, during this assembly of convection terms into Eq. (22), integration point values such as integration point velocities, $u_{k,ip1}$ and $v_{k,ip1}$, still must be related to nodal variables, such as $U_{k,1}, V_{k,1}$ and $P_{k,1}$, in order to provide a well-posed algebraic system. Conventional schemes, such as UDS (Upwind Differencing) or CDS (Central Differencing), often lack a complete coupling between problem variables at the integration point. As a result, an alternative scheme (PINS, or Physical INfluence Scheme) is adopted here at an integration point level for multiphase flows.

### 3.3. Integration point equations

In the current PINS approach, the integration point values are determined from a local balance of transport processes at that location and related to entropy principles (Naterer, 1999). In particular, the integration point velocity components (air and droplets separately) are obtained from the transport forms of the momentum equations, corresponding to Eq. (22). For the main (air) flow in the $x$ and $y$ directions, respectively,

$$\rho\frac{\partial u}{\partial t} + \rho u\frac{\partial u}{\partial x} + \rho v\frac{\partial u}{\partial y} = -\frac{\partial p}{\partial x} + \mu\left(\frac{\partial^2 u}{\partial x^2} + \frac{\partial^2 u}{\partial y^2}\right) + \hat{S}_x, \tag{28}$$

$$\rho\frac{\partial v}{\partial t} + \rho u\frac{\partial v}{\partial x} + \rho v\frac{\partial v}{\partial y} = -\frac{\partial p}{\partial y} + \mu\left(\frac{\partial^2 v}{\partial x^2} + \frac{\partial^2 v}{\partial y^2}\right) - \rho g + \hat{S}_y, \tag{29}$$

where $u, v, p, \mu, \rho$ and $g$ refer to $x$ direction velocity (air), $y$ direction velocity, pressure, dynamic viscosity, air density and gravitational acceleration, respectively. The source terms, $\hat{S}_x$ and $\hat{S}_y$, in these equations refer to inter-phase forces, particularly interactions between the droplet and air streams.

It can be observed that the integration point equations involve the following five distinct operators: transient (1st term), convection (2nd and 3rd terms), pressure (4th term), diffusion (5th and 6th terms) and source terms (7th term). The solutions for the integration point velocity components are obtained by a suitable discrete approximation of each of these operators. These operators (in order) are approximated by a backward difference in time (transient), upstream differencing (convection), bilinear interpolation of nodal values (pressure), central differencing (diffusion) and bilinear interpolation (sources/sinks) (Naterer, 1999).

Based on these operators, the following discrete approximation of Eq. (28) at an integration point (subscript ip) is obtained:

$$\frac{u_{\mathrm{ip}}^{n+1} - u_{\mathrm{ip}}^{n}}{\Delta t} + \rho V\left(\frac{u_{\mathrm{ip}}^{n+1} - u_{\mathrm{u}}^{n+1}}{L_c}\right) = -\sum_{j=1}^{4} \frac{\partial N_j}{\partial x} P_j^{n+1} + \frac{\mu}{L_{\mathrm{d}}^2}\left(\sum_{j=1}^{4} N_j U_j^{n+1} - u_{\mathrm{ip}}^{n+1}\right) + \hat{S}_x^{n+1}, \tag{30}$$

where the diffusion length scale is given by

$$L_{\mathrm{d}}^2 = \left(\frac{2}{\Delta x^2} + \frac{8}{3\Delta y^2}\right)^{-1}. \tag{31}$$

In Eq. (30), the superscripts $n+1$ and $n$ refer to current and previous time levels, respectively. The convection operator has been approximated by a skewed upwind difference (i.e., upwinding to edge of element based on local flow direction). Also, $V = \sqrt{u^2 + v^2}, L_{\mathrm{c}}$ and $u_{\mathrm{u}}$ represent the fluid velocity magnitude, convection length scale (distance to upwind edge) and upwind value of $u$, respectively. The direction of the line between the integration point and upwind value of $u$ is defined by the local velocity components about these locations. Although Eq. (30) is given in the $x$ direction, a similar result is obtained for the $y$ direction integration point equation.

Following this substitution of discrete operators into Eqs. (28) and (29), a local matrix inversion is required to express the four integration point values (per element) in terms of nodal values alone. These inverted matrices provide the coupling between integration point and nodal point values. They are adopted in the control volume equations to evaluate the sub-surface convection terms and thus complete the closure of the discrete equations. In other words, a discrete approximation of the governing differential equations is solved at each integration point to give an accurate representation of the convected quantities in Eq. (22). This approximation is solved for the main unknown, integration point velocity, in terms of nodal values of velocity and pressure.

The dependence between integration point and nodal point variables is expressed through *influence coefficients*, which are similar to the leading coefficients of temperature due to interpolation alone in the diffusive terms, i.e., Eq. (27). Once the integration point velocities are substituted into Eq. (25) and subsequently Eq. (22), the convective flux terms are completed for a particular sub-surface. Then, similar calculations are performed at the other sub-surfaces to complete the contributions of convection for each of the four sub-control-volumes within an element.

A set of simultaneous equations for pressure, $p$, and velocity, $v$, is obtained in Eq. (22) in the mass and momentum equations since the substituted integration point velocities depend on both velocity and pressure. For example, in the continuity equation, pressure appears through the dependence of integration point velocity on pressure in Eq. (22). Similarly, pressure appears in the momentum equations through both convective and pressure gradient terms. As a result, once the control volume equations are solved simultaneously, the pressure distribution throughout the flow field is predicted. Iterations are typically carried out until convergence between the convected velocity (solution of momentum equation) and convecting velocity (integration point, mass conserving velocity) is achieved.

In addition to integration point equations for the main (air) flow, similar equations are solved for the droplet flow. The droplet velocities are particularly important in terms of the mass influx of droplets into control volumes located along the moving gas/solid interface. The following $x$ direction transport equation for droplets is based on the momentum equation in the liquid (droplet) phase, Eq. (16), i.e.,

$$\hat{\rho}_l \frac{\partial u_l}{\partial t} + \hat{\rho}_l u_l \frac{\partial u_l}{\partial x} + \hat{\rho}_l v_l \frac{\partial u_l}{\partial y} + \langle \dot{m}'' u_l \rangle_i = C_l \langle G_{x,l} \rangle. \tag{32}$$

The resistance term may be expressed by Eq. (14) from which the following quasi-steady approximation of the droplet equation is obtained:

$$u_l \sum_{i=1}^{4} \frac{\partial N_i}{\partial x} U_{l,i} + v_l \sum_{i=1}^{4} \frac{\partial N_i}{\partial y} U_{l,i} = \frac{18\mu_a}{\rho_l d^2} \frac{c_{\mathrm{d}}}{24/Re} (u_a - u_l)^{\gamma}, \tag{33}$$

where $\gamma$ is the empirical resistance term exponent (based on Hewitt et al., 1997). The term involving evaporation and coalescence (last term in Eq. (32) on left-hand side) is neglected due to its assumed small contribution in comparison to droplet inertia. Although the transient term is not included in Eq. (33), the full coupling with the control volume flow equations provides a temporal variation of the flow field and ice buildup. Also, it should be noted that the present formulation assumes that the incoming droplet velocities at the inflow boundary remain uniform in time.

## 4. Numerical procedures

In addition to the previously described numerical discretization, other steps must be taken in the numerical algorithm to provide effective performance. These additional steps involve the moving phase interface(s). Solidification of incoming supercooled droplets will change the surface's shape due to the resulting ice accretion. Moving boundary problems, such as this ice phase change problem, involve a discrete change of the phase interface position at each time step. Grid transformations to accommodate this moving boundary generally entail difficulties such as interpolation of scalar values from the previous grid to new nodal locations on the updated grid. Furthermore, grid and coordinate transformations are time-consuming and difficult to incorporate into conventional CFD codes using a fixed domain. As a result, it is worthwhile to consider an alternative, fixed domain algorithm capable of handling the droplet dynamics, as well as the growing ice surface once droplets have been deposited on the surface.

In the current approach, the droplet content or distribution in the flow field is modelled through the scalar transport equation for the droplet's liquid (water) content. In a control volume along a solid wall or ice surface, the droplet flow is altered due to the presence of the surface. Furthermore, freezing of the impinging droplets upon impact increases the solid fraction of the volume (potentially consisting of air, liquid and solid ice). If a sufficiently large mass influx leads to a filled control volume (i.e., filled with water and/or ice), then the air flow no longer passes through this occupied volume and the edge of the ice interface moves into an adjacent control volume. In this way, the liquid fraction within a volume, as well as the surface location itself, are both used to identify the location of the moving ice surface.

At the solid (ice) surface, incoming droplets can accumulate until the control volume at the surface becomes filled. Beyond this point, the water (liquid and/or solid) fraction becomes one and the advective term in the scalar transport equation is reduced to zero for this filled volume. The position of the ice interface is identified now by the adjacent volume containing a liquid fraction between 0 and 1. As a control volume changes phase from partially filled to completely filled, the amount of droplet influx into the partially filled volume may exceed the volume available. As a result, the volume becomes filled and the excess amount is transferred to the adjacent control volume for proper mass conservation. The phase fraction is a bounded scalar (between 0 and 1) and so a droplet influx into a nearly filled volume must not surpass this bound.

As the interface moves from one volume to an adjacent volume, the excess mass ('overfilled' amount) from the former control volume is implicitly added to the adjacent volume once the phase change is effected in the following iteration (or time step). In this way, mass conservation is achieved. However, another difficulty is realized if the ice (solid–air) interface moves more than two control volumes (or elements) away from its present position because a direct connection between nodes is no longer apparent. In this instance, a time step limitation is required for numerical stability. However, this limitation is generally much less stringent than conventional time step limitations, such as the CFL condition (Anderson et al., 1984), as a result of the typically small liquid water content (i.e., large time to fill a control volume). Furthermore, in practice, a reduced time step may provide a more efficient solution advance than multiple iterations within a larger time step, due to the interactions with other non-linearities, including convection, phase change and droplet impingement.

Before the control volume is filled, the complete mass inflow and outflow terms are applied (based on conservation of mass in air and liquid phases). However, once the control volume becomes filled, the mass inflow is reduced. In particular, as the phase fraction (i.e., water and/or ice) approaches one, the mass inflow term is reduced to zero through multiplication by a phase fraction weighted scaling factor. Although this process is already included in the thermal and fluid physics, numerical iterations are generally required to achieve proper convergence. Thus the inter-equation coupling is strengthened by this weighting factor without a loss of generality. Since the scaling factor remains as one throughout the flow period but abruptly falls to zero once the liquid fraction becomes one, it maintains the regular flow equations until the control volume is filled. After the control volume is filled with liquid from the droplets, the computational effort is reduced as a result of the de-coupling in the discrete equations. In this procedure, a zero air flow velocity is properly predicted in the ice.

The finite element framework of the numerical formulation provides the geometric flexibility of the simulations. An unstructured mesh is utilized, in contrast to conventional finite volumes, which are typically based on structured grids involving a row/column format. Also, the discrete equations are developed in isolation and independent of the mesh configuration. The usual type of finite element assembly rules are used to re-construct the whole domain from its parts (elements). Furthermore, the computer algorithm is based on standard finite element procedures, with the exception that local stiffness equations are based on control volume balances, rather than other conventional techniques such as Galerkin weighted residuals.

## 5. Experimental apparatus and procedures

Experiments involving aerodynamic measurements with iced cables (Stumpf and Ng, 1990) and freezing precipitation (Lu et al., 1998) have been performed at the University of Manitoba. The outdoor freezing simulator includes spray nozzles, a fan and a short horizontal conductor placed perpendicular to the airstream produced by the fan. Droplets are sprayed onto the sample from a set of spray nozzles supplied with pre-cooled water. In the currently illustrated data, these nozzles supplied droplets with a mean volume diameter of about 1 mm. By placing the freezing rain simulator in an outdoor space surrounded by several buildings, interference from the ambient wind was reduced. An anemometer was used to measure the air speed produced by the fan and a weight scale and microscope were used to measure the size spectrum of the water droplets. Furthermore, the vertical and horizontal components of precipitation were measured with two precipitators.

Although the droplet temperatures needed to stay slightly above 0 °C at the nozzle exit to prevent freezing within the supply tubes, efforts were taken to supercool the water further by spraying the droplets about 10 m high prior to their falling onto a conductor sample. In this way, the travel distance of the droplets was viewed to be sufficient to allow the droplets to match the ambient air temperature closely. The mass of ice accretion was recorded at different times through a plaster cast sample replicated from the ice shape, and later traced out to estimate an area (and thus mass) around the conductor. Alternatively, by placing the sample in a liquid container and measuring the resulting displaced liquid volume, the resulting volume could be converted to an equivalent mass. Based on tests involving comparisons between stranded cables and smooth cylinders, it was observed that the effects of a conductor's stranding on the ice shape and weight seemed minor.

The experimental uncertainties in these tests were largely due to the measurement of precipitation rate. Measurements of vertical and horizontal components of precipitation, as well as air speed and air temperature, were recorded at half hourly intervals. The liquid water content was not measured directly, but rather, it was computed through the measured precipitation rate and wind velocity. By performing comparable experiments over shorter time intervals, it was estimated that the maximum error in the measured precipitation rate (and thus liquid water content) was about ±10%. Furthermore, the measurement accuracy involving ice thickness was limited by some three-dimensional icing variations along the cable. Additional comparisons with actual ice samples from a power line after a freezing rain storm indicate that the experimental simulations possessed comparable characteristics in comparison to the actual iced cables. As a result, it is anticipated that the experimental results provide good representation of actual power line icing in outdoor conditions.

## 6. Results and discussion

### 6.1. Impinging droplets on planar surface

An example problem involving a one-dimensional droplet flow is considered here for basic validation of the droplet flow formulation. It may be viewed as droplets falling at their terminal velocity in quiescent air (see Fig. 3). Alternatively, it may be considered as droplets flowing in a horizontal direction ($x$ direction) and impacting on a wall. In rime (dry) ice conditions, droplet freezing occurs immediately upon impact. Consider droplets initially located at $x = 0$ (dimensionless), and moving toward a wall ($x = X$) at a uniform velocity, $u$. An analytical solution for the interface position, $\lambda$, in terms of time, $t$, droplet velocity, $u$, and volume fraction of droplets in air, $C_l$, can be shown to be

$$\lambda = X - \left(t - \frac{X}{u}\right)uC_l; \quad t \geqslant \frac{X}{u}. \tag{34}$$

Physically, the rate of mass accumulation on the ice surface balances the rate of incoming mass flow onto the ice surface. The time duration before droplets arrive at the surface is $X/u$ and the interface only begins to grow after this time. It is assumed that air motion is not altered at the moving ice interface (horizontal orientation), or alternatively, the droplets fall at their terminal velocity in quiescent air (vertical orientation).

A demonstration of some basic features of the formulation may be observed through the discretization of the following 1-D form of the droplet equation

$$\frac{\partial C_l}{\partial t} + \frac{\partial}{\partial x}(uC_l) = 0, \tag{35}$$

where $C_l$ refers to the volume fraction of droplets in air. Discretizing Eq. (35), based on a backward difference in time, together with direct upwinding,

$$\left(\frac{C_{l,i}^{n+1} - C_{l,i}^{n}}{\Delta t}\right)\Delta x + (\eta_i u_i C_{l,i}) - (\eta_{i-1} u_{i-1} C_{l,i-1}) = 0, \tag{36}$$

where the subscripts $i - 1$ and $i$ refer to the upstream node and the node centered within the control volume, respectively. Also, the superscript $n$ refers to the previous time level.

A mass weighting factor, $\eta$, is adopted for damping the mass influx into a filled control volume, where

$$\eta = 2 - \frac{2}{1 + \lambda^{0.1}}. \tag{37}$$

The use of this weighting factor is not intended to arbitrarily re-distribute mass along the phase interface. Instead, it is intended to serve as a technique of numerically blocking out any additional

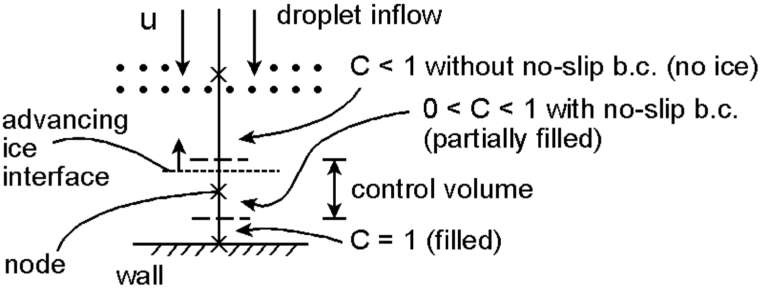

Fig. 3. Schematic of 1-D droplet impingement problem.

droplet mass flow into an already filled control volume. In this way, it represents a step function to only permit a maximum amount of mass into the control volume. Otherwise, a mass 'overflow' would need to be re-distributed to surrounding control volumes, which would defeat the purpose of the overall three-phase approach, since interface tracking in the adjacent control volumes would need to be pursued. Once the droplet influx fills the control volume along the moving boundary, $\eta$ rises abruptly to retain the excess mass within the control volume from where the droplets arrived. Inter-equation iterations are performed to ensure that the mass retained by the control volume adjacent to the filled volume along the phase boundary balances the mass excluded from the filled control volume. It can be observed that $\eta \to 0$ abruptly when the control volume is filled ($\lambda \to 1$). In this way, the inter-equation stability involving the droplet and air flow equations is also improved. Thus, the use of $\eta$ represents a novel new technique for conservation of mass within the framework of a fixed grid, three-phase methodology. Furthermore, a distinction between droplet fraction in an air–droplet control volume (denoted by $C_l$) and liquid fraction in a solid–liquid control volume is established in the event of extending this formulation to glaze ice conditions.

In Eq. (36), an implicit solution of the resulting algebraic equations may be readily obtained. For illustration purposes, consider a four-node discretization, i.e.,

$$C_{l,1} = C_{l,\text{in}}, \tag{38}$$

$$C_{l,2} = \frac{C^n_{l,2} + C_{l,\text{in}}\eta_2 Co}{1 + \eta_3 Co}, \tag{39}$$

$$C_{l,3} = \frac{C^n_{l,3}}{1 + \eta_4 Co} + \frac{\eta_3 Co(C^0_{l,2} + C_{l,\text{in}}\eta_2 Co)}{(1 + \eta_4 Co)(1 + \eta_3 Co)} = C_{l,4}, \tag{40}$$

where $Co = u\Delta t/\Delta x$ refers to the Courant number and $C_{l,\text{in}}$ is a specified value at the boundary inlet. The first equation for node 1 represents a boundary (inflow) condition. Also, as more nodes are considered, the anticipated pattern of subsequent nodal $C_l$ values can be observed from Eqs. (39) and (40). A preliminary investigation of this solution (i.e., selecting sample values of $\Delta x$, etc.) shows that the control volumes become successively filled ($C_l \to 1$) over time as expected. In this approach, a situation may arise where a fine grid resolution near the boundary may initiate an interface advance beyond 2–3 control volumes in a single time step and iteration. In this situation, convergence difficulties may be avoided by reducing the time step size. In the above example, the recommended condition is $C_{l,\text{in}} u\Delta t/\Delta x < 1$. This condition resembles the conventional CFD stability criterion for explicit schemes (i.e., $Co \equiv u\Delta t/\Delta x < 1$), but it is generally much less restrictive, since the liquid water content in the flow field is generally much less than unity (i.e., $C_{l,\text{in}} \ll 1$).

The previous analysis has considered a coarse grid (i.e., three nodes plus fourth node at wall) to show some overall algorithm features. At this stage, a more suitable grid refinement will be examined (i.e., 4 × 10, 4 × 15 and 4 × 20 elements). In Fig. 4(a) and (b), results are displayed for the ice interface movement over time, with a focus on sensitivity to time step and grid spacing. The interface movement is delayed (see upper left portion of graph where position remains at 1) since some time must elapse prior to the initial impact of the freestream droplets on the surface. After this instant, it can be observed that the predictions come within close agreement with the solution given in Eq. (34), particularly as the time step is reduced and the grid is refined.

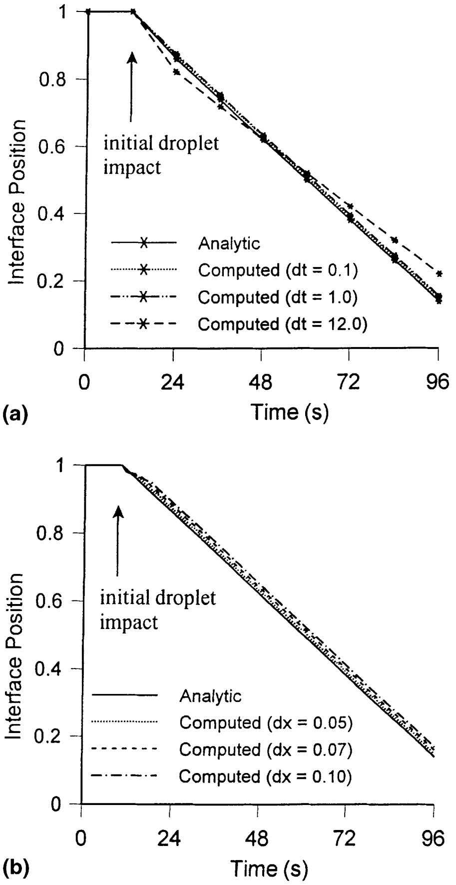

Fig. 4. Phase interface results with (a) time step and (b) mesh refinements.

### *6.2. External droplet and viscous air flow past iced conductor*

In this problem, a 2-D external viscous flow is predicted in conjunction with a moving phase interface arising from impinging supercooled droplets and ice accretion on a cable. The practical importance of this problem is its application to icing of overhead power transmission lines. In addition to predicting conditions leading to potential structural damage, such as excessive ice and wind loads, or power line galloping, the current predictive model can be used as an effective design tool in maintaining a reliable power supply during harsh weather conditions.

In the current problem, a combined air–droplet flow and ice accretion is predicted in conditions with an initially bare (uniced) cable diameter of 2.86 cm, ambient air temperature of −8.2 °C, incoming wind velocity of 13 m/s and precipitation rate of about $1.2 \times 10^{-3}$ mm/s (note: droplets carried by wind horizontally at inflow boundary). In Fig. 5, a schematic of the external flow past the cable and a sample domain discretization are illustrated. This problem is considered to be representative of typical precipitation and air flow conditions leading to atmospheric icing of overhead power lines, whereby rime (dry) ice accumulation is observed at sub-zero temperatures.

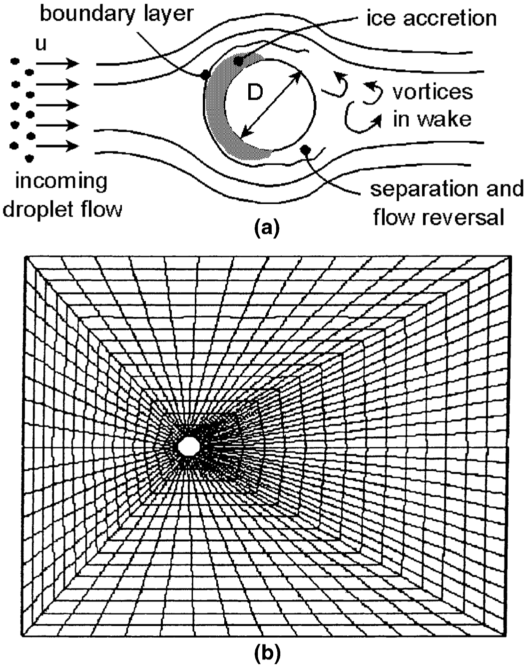

Fig. 5. (a) Schematic of 2-D droplet impingement problem with (b) sample mesh discretization.

Under the present conditions, it is anticipated that the boundary layer remains laminar on the upstream side of the cable and separation of the boundary layer occurs with turbulence in the downstream wake. The detailed impact of turbulence was not examined since downstream flow processes were viewed to have a minor effect on the main parameter of interest here (mass of ice buildup on upstream side of cable). For nearly symmetrical iced cables, which typically arise under rime ice conditions for a non-rotating conductor, experimental studies have revealed that ice accretion occurs mainly on the upstream side where the boundary layer remains laminar, despite the downstream turbulent wake. Nevertheless, a turbulent viscosity based on mixing length theory was adopted. This approach used a turbulent viscosity in addition to the molecular value in the mean flow momentum equations. It will be shown that this approach provided reasonable agreement between the numerical predictions and corresponding experimental data in terms of ice shape and mass.

In Figs. 6 and 7, the transient predictions of ice growth, ice shape and air velocity (depicted by velocity vectors) are shown. The ice surface is represented by phase fraction contours at the advancing interface as it grows into the wind. Since the non-air phase fraction (i.e., liquid droplets and/or ice) is plotted, the contours essentially track the droplet trajectories, as well as the ice accumulation on the cable surface. For example, at the inflow boundary, this phase fraction is equivalent to the liquid water content. The scalar transport equation for this phase fraction is solved, in conjunction with the droplet momentum and main (air) flow equations, to track the droplet distribution through the flow field.

If the intervals between the phase fraction contour labels are sufficiently small (i.e., within the range of the freestream's liquid water content), then the results would actually depict the droplet

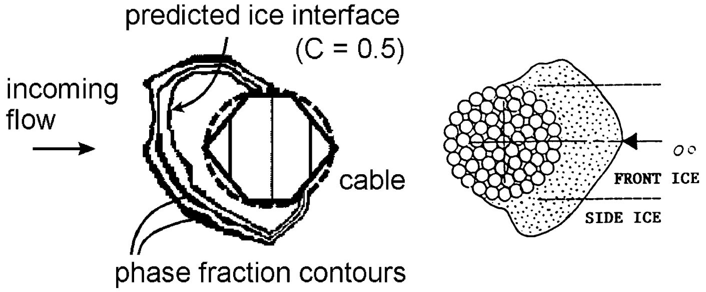

Fig. 6. (a) Predicted and (b) measured results of ice shape ($t^* = 0.788$).

movement throughout the domain. However, this labelling would then be too fine to capture the much larger (order of 1) phase fraction at the solid boundary as it represents the growing ice interface. If it is desired, then the contour labelling could be specified within the liquid water range of the freestream droplets, or surface liquid–ice, to examine the droplet flow or ice accretion, respectively. In the former case, all relevant droplet dynamics, including deflection by the air stream, collection efficiency at the cable surface (i.e., the surface's ability to 'capture' droplets), and impingement at the solid boundary, are simulated.

In the comparisons between computed results and experimental data, a dimensionless ice thickness, $\delta^*$, and dimensionless time, $t^*$, will be used. These variables are defined as follows:

$$\delta^* = \frac{\delta}{R}, \tag{41}$$

$$t^* = 2\frac{\rho_w}{\rho_i}\frac{Pt}{\pi R}, \tag{42}$$

where $t$, $P$ and $R$ refer to time (from the start of the freezing precipitation), precipitation rate and cable radius, respectively. The equivalent ice thickness, $\delta$, is defined as the uniformly radial ice thickness having the same equivalent mass of ice as that observed.

In Fig. 6, the predicted ice profile is illustrated and compared with a measured ice shape obtained at the same dimensionless time ($t^* = 0.788$). Although this represents a range of possible wind velocities and liquid water contents yielding the same value of $t^*$ (but at different times), the shape of ice is often mainly dependent on $t^*$ under dry (rime) ice conditions when droplets freeze immediately upon impact without droplet splashing. Additional numerical simulations have verified that close similarity of ice shapes is obtained at identical values of $t^*$ even though the wind velocity and liquid water content are slightly different. It can be seen that fair agreement between the predicted and experimental results is achieved in Fig. 6. The notable features of the predictions include both side and frontal ice growth.

Although the frontal growth is well understood, the mechanisms responsible for accumulation along side elements is less understood. It is anticipated that the component of the surface tangent of the boundary element in the direction of the incoming precipitation is responsible for a portion of the droplets captured by the surface. Furthermore, since the droplet mass is lumped within a control volume (i.e., approximated by a single effective droplet mass smeared across the volume), then a portion of the droplets passing by the side sections of the conductor is captured while the

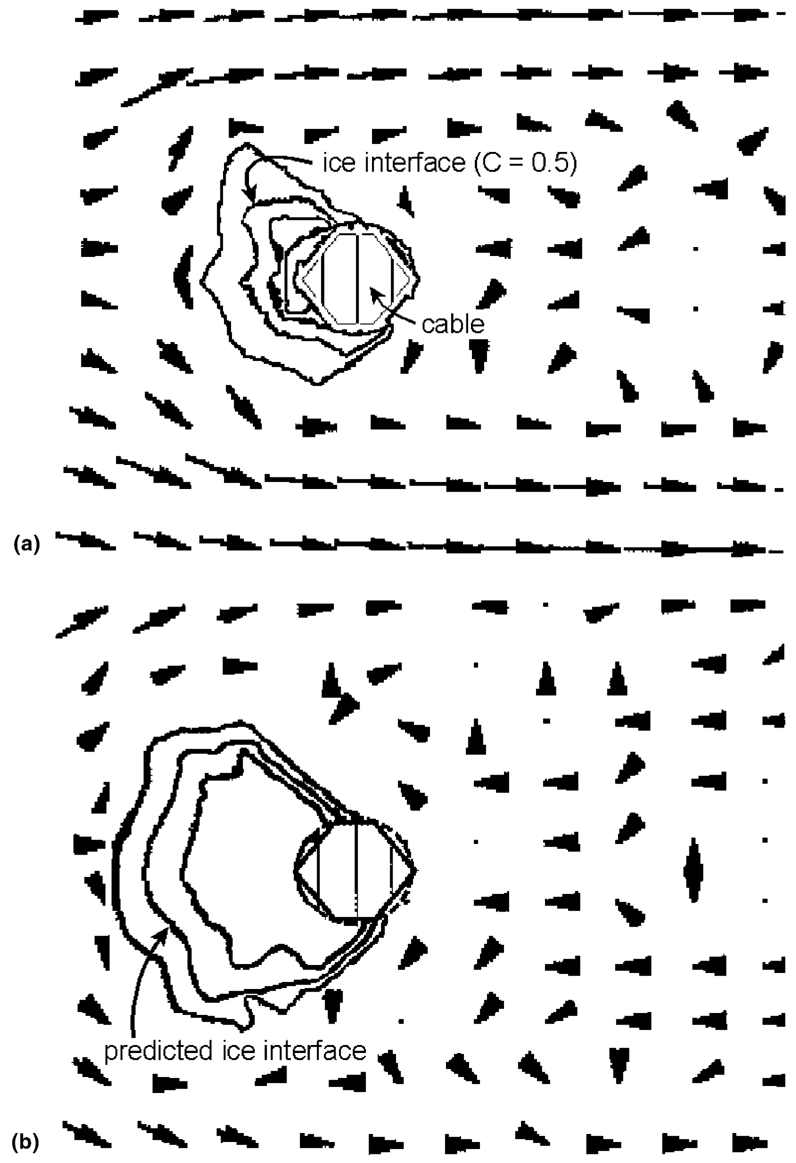

Fig. 7. Predicted results at (a) $t = 6$ h and (b) $t = 12$ h.

remaining portion exits the control volume past the conductor. In any case, it appears that important physical processes involving droplet capturing have been modelled in the current work.

In Fig. 7(a), the ice accumulation is depicted after 6.0 h. Although the simulations are performed on an unstructured finite element mesh, the velocity vectors are displayed at a uniform spacing. Also, the circular conductor is approximated by straight-line segments, and these segments are enclosed within a shaded ‘pixel’ region. Furthermore, it should be noted that results from the unstructured (finite element) mesh are interpolated onto the output graphs which use a structured (row and column) format. In Fig. 7(a), the velocity magnitudes are scaled in accordance with a reference velocity. Also, dots in the flow field refer to small velocity magnitudes. In the case of regions within the ice accretion, these dots correctly depict zero velocities, since the non-zero phase fraction in the main (air) flow equations damps any resulting air velocities to zero there.

An important part of the predictions involves the recirculating flow behind the iced cable. Boundary layer separation and flow reversal are indicated by the left and/or down facing velocity vectors near the downstream upper and lower cable regions, respectively. Shedding of vortices is created in this downstream region and the width of the wake increases as ice growth occurs at the top and bottom edges of the cable (i.e., there is an increasingly exposed area normal to the flow direction). It should be noted that for rime ice with no cable rotation, the effect of downstream flow structures (i.e., vortex motion, wake) on the main parameter of interest (mass of ice accretion) seems minor. This minor effect can be observed since droplets adhere immediately upon impact with no splashing and a high incoming air inertia implies that the droplet and air velocities are not appreciably different.

Despite this anticipated small effect on the mass of ice, a slight asymmetry in the shape of ice is observed. It may have occurred from the interactions between the droplets and the main (air) flow's asymmetry due to periodic shedding of upper and lower vortices along the downstream side of the cable. It should be noted that there are two widely different time scales in this problem (i.e., large-scale for ice accretion; small-scale for downstream vortices). The time scale associated with the ice accretion is selected in the time step since this phenomenon is the main focus in the present work.

In Fig. 7(b) ($t = 12$ h), even more ice accumulation is observed together with its effects on the surrounding air–droplet flow. In these results, an important contribution of the present work is achieved in that both side ice and frontal ice are predicted. Other studies have typically predicted mainly frontal ice, which does not agree with this experimental data that shows side ice, and as a result, the mass of ice would be underpredicted. Otherwise, other researchers have used empirical geometrical factors (without coupling to the flow solution) to place mass at the side of the conductor. But, models which correctly predict the mass of ice often overpredict the frontal ice in compensation for not properly accounting for side ice. This problem arises when the moving ice boundary problem is not implicitly coupled to the external multiphase flow solution. The current work appears to reasonable predict this side ice growth based on the problem physics directly. This side ice growth is predicted in conjunction with the viscous multiphase flow around the conductor.

The actual ice interface is approximated by the 0.5 contour since this contour approximates the midpoint between a filled control volume and a completely unfilled control volume (where unfilled refers to ice). At subsequent times, the continued ice growth is predicted, together with its effects on the flow patterns on both upstream and downstream sides of the conductor. In the simulations, 20 time steps were used to reach 12 h of actual (physical) time (note: smaller time steps were used in the time step refinement studies) . Also, grid discretizations of 441 nodes (184 elements), 671 nodes (600 elements), 1104 nodes (1020 elements) and 2541 nodes (2400 elements) were used. Solution convergence within each time step (1104 node mesh) was typically achieved within 20–30 s on a 500 MHz laptop computer. In view of the complexity of this three-phase problem (i.e., mass and momentum equations for droplets and air flow, mass conservation with impinging droplets at ice surface, etc.), this computational effort indicates economical performance. As a result, it is viewed to be a promising tool for problems involving multiphase flows.

Another aspect of validation is a comparison with experimental results involving change of mass of ice accretion with respect to time. Previous studies (Lu et al., 1998) indicate that the ratio of dimensionless ice thickness, $\delta^*$, to time, $t^*$, should remain constant at approximately one-half (assuming an unheated, non-rotating conductor). This analytical prediction, as well as the experimental data and current computed results are depicted in Fig. 8. Favorable agreement is observed between these results. The experimental data was obtained over a variety of atmospheric conditions. Based on these favorable comparisons, it appears that the current models are capable of reasonably predicting both ice weight and shape during freezing precipitation.

Additional results are shown in Fig. 9(a) and (b). Sensitivity studies for grid spacing and time step refinements are shown in Fig. 9(a). In both cases, the dimensionless ice thickness to time ratio is computed (at $t = 12$ h) and compared with the analytic solution of Goodwin et al. (1982), which agrees well with experimental data. The Courant number is defined as $Co = u\Delta t/\Delta x$ along the horizontal axis and $u = 13$ m/s (incoming velocity) in this case. It can be observed that for both the time step refinement (solid line; $Co$ decreases as $\Delta t$ decreases) and grid refinement (dashed line; $Co$ increases as $\Delta x$ decreases), the results approach the analytic ratio of 0.5. It should be noted that the grid spacing was defined as the average $\Delta x$ in the upstream region between the leading edge of the cable and the inflow boundary. Thus, the range shown in Fig. 9(a) actually depicts a wide range of mesh discretizations between 441 and 2541 nodes.

In Fig. 9(b), the dimensionless ice thickness, $\delta^*$, at $t = 12$ h, is shown under different flow conditions. In the first case, the incoming wind velocity is maintained constant ($V = 13$ m/s), but the liquid water content is varied to give a range of precipitation rates. In the second case, the liquid water content is maintained constant ($G = 0.065$ g/m$^3$) and the wind velocity is varied independently (results plotted with square data markers). It can be observed that the ice thickness increases nearly linearly with precipitation rate. It can be shown that the results in Fig. 9(b) also

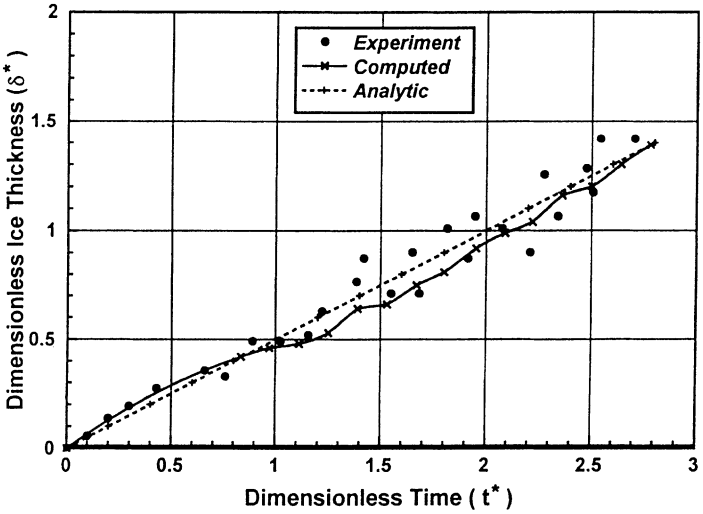

Fig. 8. Predicted and measured results of ice mass.

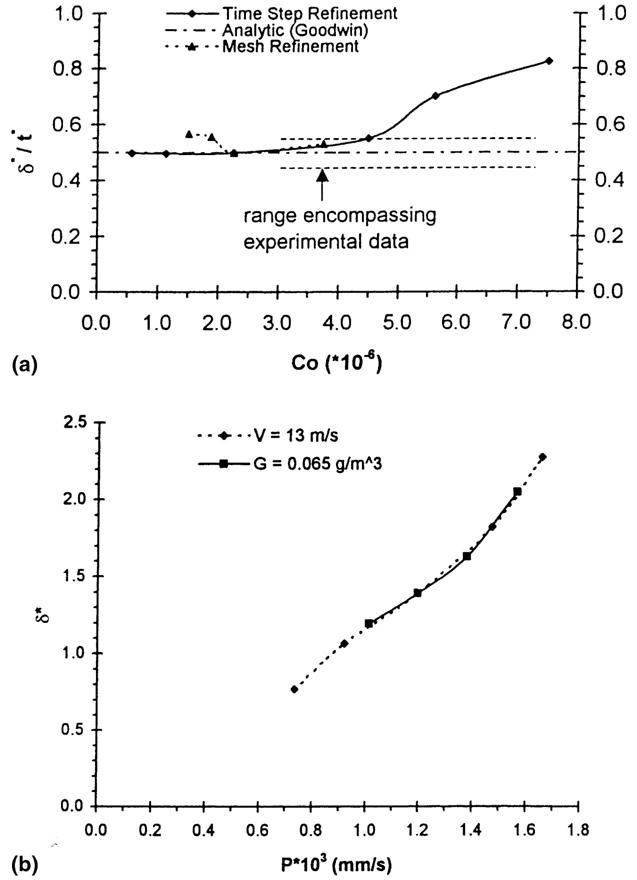

Fig. 9. (a) Grid and time step refinement and (b) other flow conditions.

agree closely with the experimental range of ice buildup (rime ice conditions) of $\delta^* \approx t^*/2$. For example, $\delta^* \approx 0.48t^*$ for the leftmost data point shown in Fig. 9(b). These results illustrate the simulation capabilities of the present formulation over a fairly wide range of flow conditions.

## 7. Conclusions

Multiphase flows with droplets in three-phase conditions (air, droplets and ice) have been examined in the present paper. The Navier–Stokes equations and equations of droplet motion are discretized with a CVFEM to predict the main (air) flow and droplet velocities. Interactions between the droplet and air flows appear through appropriate inter-phase correlations in the momentum equations. The spatial distribution of droplets throughout the domain is predicted by a scalar transport equation involving phase fraction. It is anticipated that this Eulerian approach provides an effective alternative to Lagrangian tracking of individual droplet trajectories. Phase change of impinging droplets, together with their solidification and effects on boundary layer separation in the surrounding viscous flow, are presented and discussed. Based on favorable comparisons between experimental data and the numerical predictions, it is viewed that the current formulation provides an effective design tool for problems involving multiphase flow with droplets and ice accretion.

## Acknowledgements

The contributions of Dr. N. Popplewell and Mr. W. Barrett at the University of Manitoba are appreciated. Financial support from Manitoba Hydro for this research is gratefully acknowledged, and in particular, the assistance and support of Mr. J. Chan is appreciated. Also, financial support from the Natural Sciences and Engineering Research Council of Canada is gratefully acknowledged.

## References

Anderson, D.A., Tannehill, J.C., Pletcher, R.H., 1984. Computational Fluid Mechanics and Heat Transfer. Hemisphere, Washington, DC.

ASCE Manual 74, 1991. Guidelines for Electrical Transmission Line Structural Loading. American Society of Civil Engineers, New York.

Banerjee, S., Chan, A., 1980. Separated flow models – I. Analysis of the time averaged and local instantaneous formulations. Int. J. Multiphase Flow 6, 1–24.

Bankoff, S.G., 1960. A variable density, single fluid model for two-phase flow with particular reference to steam-water flow. ASME J. Heat Transfer 82, 265–272.

Desai, Y.M., Yu, P., Shah, A.H., Popplewell, N., 1996. Perturbation-based finite element analyses of transmission line galloping. J. Sound Vib. 191, 469–489.

Draganoiu, G., Lamarche, L., McComber, P., 1996. A computer model of glaze accretion on wires. ASME J. Offshore Mech. Arctic Eng. 118, 148–157.

Drew, D.A., Lahey, R.T., 1993. Analytical modelling of multiphase flow. In: Roco, M.C. (Ed.), Particulate Two-Phase Flow. Butterworth–Heinemann, London, p. 593.

Fink, D.G., Beaty, H.W., 2000. Standard Handbook for Electrical Engineers, fourteenth ed. McGraw-Hill, New York.

Goodwin, E.J., Mozer, J.D., Di Gioia, A.M., Power, B.A., 1982. Predicting ice and snow loads for transmission lines. In: Proceedings, 1st IWAIS, pp. 267–273.

Hewitt, G.F., Shires, G.L., Polezhaev, Y.V., 1997. International Encyclopedia of Heat and Mass Transfer. CRC Press, Boca Raton, FL.

Lahey, R.T., Drew, D.A., 1979. Application of general constituitive principles to the derivation of multidimensional two-phase flow equations. Int. J. Multiphase Flow 4, 243–264.

Lu, M.L., Popplewell, N., Shah, A.H., Barrett, W., Au, A., 1968. Mass of ice accretion from freezing rain simulations. In: Proceedings, Eighth International Workshop on Atmoshperic Icing of Structures, Reykjavik, Iceland.

Myers, T.G., Hammond, D.W., 1999. Ice and water film growth from incoming supercooled droplets. Int. J. Heat Mass Transfer 42, 2233–2242.

Naterer, G.F., Deng, H., Popplewell, N., 1999. Predicting and reducing glaze ice accretion on electric power lines with joule heating: theory and experiments. CSME Trans. 23, 51–70.

Naterer, G.F., Schneider, G.E., 1995. PHASES model of binary constituent solid–liquid phase change: Part 1 – numerical method. Numer. Heat Transfer B 28, 111–126.

Naterer, G.F., 1999. Constructing an entropy-stable upwind scheme for compressible fluid flow computations. AIAA J. 37, 303–312.

Nigol, O., Havard, D.G., 1978. Control of torsionally-induced conductor galloping with detuning pendulums. IEEE Paper A 78 125-7, January.

Poots, G., 1996. Ice and Snow Accretion on Structures. Wiley, New York.

Stumpf, P., Ng, H.C.M., 1990. Investigation of aerodynamic stability for selected inclined cables and conductor cables. B.Sc. Thesis, Department of Mechanical and Industrial Engineering, University of Manitoba, Winnipeg.

Szilder, K., Lozowski, E., Gates, E., 1987. Modelling ice accretion on non-rotating cylinders – the incorporation of time dependence and internal heat conduction. Cold Regions Technol. 13, 177–191.

Tsuboi, K., Kimura, S., 1998. Numerical study of the effect of droplet distribution in incompressible droplet flows. In: AIAA 29th Fluid Dynamics Conference, Albuquerque, NM, AIAA Paper 98-2561.